



Trajectory tracking of an oscillating movement with a low-cost IMU in geodetic surveying applications

Gašper Štibe^{a,*}, Peter Krapež^b, Janez Podobnik^b, Dušan Kogoj^a

^a Faculty of Civil and Geodetic Engineering, University of Ljubljana, Jamova cesta 2, 1000 Ljubljana, Slovenia

^b Faculty of Electrical Engineering, University of Ljubljana, Tržaška cesta 25, 1000 Ljubljana, Slovenia

ARTICLE INFO

Keywords:

Low-cost IMU
IMU calibration
3D Trajectory Tracking
Kinematic measurements
Zero Phase Filter
Kalman Filter

ABSTRACT

In this paper, we design a method to use a low-cost IMU (Inertial Measurement Unit) sensor for the absolute positioning of an oscillating object and for improvement of the kinematic RTS (Robotic Total Station) high-precision trajectory tracking accuracy. Typically when using standard methods for position estimation based on IMU measurements, a drift of several hundred meters occurs after only 1 min of operation. When processing IMU measurements with our proposed method, which is based on the Zero-Phase filter (ZPF), the accuracy of the oscillating object's position improved to a few centimeters. We used our method to improve the RTS trajectory tracking system. By combining low-cost IMU and RTS measurements, we were able to obtain highly accurate trajectory at a frequency of IMU measurements. We improved the accuracy of the trajectory tracking compared to linear interpolation between measured RTS samples by 40% and the SNR (Signal-to-Noise Ratio) was more than three times higher.

1. Introduction

Technological progress over the last decade has led to enormous strides in MEMS (Micro-Electro-Mechanical Systems) IMU manufacturing. The size and price of IMUs are consequently decreasing, while their accuracy and performance are improving. This is a major reason for the widespread use of low-cost IMUs. In this paper, we analyze the potential applicability of a low-cost IMU for position and displacement monitoring of an oscillating objects. Displacements are, in principle, estimated by double integration of the acceleration in time. However, due to the accelerometer signal noise and other systematic errors, enormous drift can occur after double integration and the results may not be usable without additional processing. There are different approaches that researchers use for quality enhancement. The signal noise of the accelerometer can be reduced before the double integration step. In [1], the authors used the state-space approach to minimize low-frequency errors in the measured signal. In [2], the authors applied a high-pass filter to accelerations with estimated initial velocity. With the method described in [3], the noise of the accelerometer signal can be removed by a smoothing process based on the diffusion equation, which is a special partial differential equation. Under the assumption that any

accelerometer bias and gravitational acceleration is removed before further processing, these methods can significantly reduce the drift accumulated by the double integration of the accelerometer signal, especially when using high-grade accelerometers with short observation periods. Another approach obtaining useful results is to reduce the low-frequency drift not only from raw accelerometer measurements, but also from the calculated velocity and position (or displacement) of the object. With the polynomial fitting algorithm, we can eliminate trend errors after both steps of the acceleration integration. The drift of the velocity or displacement is approximated with the polynomial function and subtracted from it. The method has been well-described in [4,5]. The researchers in [6] developed the PB-algorithm based on polynomial fitting, spline interpolation, and a wavelet transform to reduce drift of position for periodic movements. Low-frequency drift can also be suppressed with different filters. The authors in [7] designed an FIR (Finite Impulse Response) filter based on a generalized minimization problem with Tikhonov regularization. The researchers in [4] developed a method for displacement reconstruction from accelerations with a LFA (Low-Frequency Attenuation) algorithm. The low-frequency drift can be eliminated with High-Pass filters, but the phase delay cannot be avoided and becomes more significant as the order of the filter increases. With a

* Corresponding author.

E-mail addresses: Gasper.Stibe@fgg.uni-lj.si (G. Štibe), Peter.Krapez@robo.fe.uni-lj.si (P. Krapež), Janez.Podobnik@fe.uni-lj.si (J. Podobnik), Dusan.Kogoj@fgg.uni-lj.si (D. Kogoj).

Zero-phase filter, we can eliminate the phase drift even when using a high-order filter. This method has been described in [8], where motion parameters and measured data derived from blast-induced vibrations were corrected with a Zero-phase filter. Researchers [9] have proposed a novel pre-compensator, which consists of a low-pass filter and a zero-phase filter, that removes the phase delay caused by the Butterworth filter.

The above-mentioned filters can successfully extract the high frequency movement, but any permanent displacements and the low frequency movements of the object are also eliminated by these correction schemes. With combination of different sensors and measurement systems, we can measure high frequency and low frequency movements. The authors in [10] presented a system that combines a high-dynamic and a low-drift sensors to address general drift problems using Kalman Filters. The authors in [11,12] proposed a method for estimating displacement through fusion of the accelerometer measurement and intermittent displacement measurements based on a Multi-rate Kalman Filter. The drift of the position can also be reduced by forward Kalman filter with backward smoothing process using the Rauch-Tung-Striebel algorithm [13]. Researchers in [14] performed a study of MEMS accelerometer-based bridge monitoring supported by an image-assisted total station (IATS). They combined IMU and 1D displacement time series with iterative extended Kalman filter (iEKF). However, the displacements or the positions estimated by Kalman filter might still contain some unresolved drift, if the intervals between KF update steps are too long. This is especially delicate when using low-grade accelerometers.

Motivated by the numerous applications of trajectory tracking systems, we explore the feasibility of using a low-cost IMU in a RTS trajectory tracking system. In this paper, we show that low-cost IMU sensors can be suitable for high-accuracy 3D trajectory tracking of an oscillating object and for improving kinematic RTS trajectory tracking. The RTS measurements guarantee absolute accuracy due to their highly accurate tracked points, while the IMU measurements guarantees relative accuracy.

First, we evaluate the quality of the standalone use of a low-cost IMU sensor for estimating the trajectory of an oscillating object using a Zero-phase filter. Next, we propose a method where preprocessed IMU trajectory and RTS kinematic tracking measurements are combined. With this approach, we increase the time resolution of the trajectory determined with geodetic RTS kinematic tracking measurements. Between the individual RTS measurements, the trajectory is smoothed by IMU measurements. The results of our proposed method are evaluated based on the comparison of measured and processed trajectories with an accurate reference trajectory. With RTS and IMU fusion, we can detect and correctly measure both low-frequency and high-frequency oscillations of the object and we are able to obtain highly accurate trajectory determined at a frequency of IMU measurements.

The aim of this paper is to develop a novel method using low-cost IMU to measure and aid at measuring the position of the oscillating objects. The novelty of this paper is twofold. First, we evaluate the quality of processing low-cost IMU measurements with zero-phase filter with sophisticated measurement system. We used a robotic arm to initiate precise motion around the starting point and measure the reference trajectory with high-accuracy Optotrak. Second, we enhanced the modern RTS Leica MS50 kinematic tracking measuring system by adding low-cost IMU measurements. We design a method for combining RTS and IMU measurements based on a zero phase filter. We compare our method of IMU and RTS fusion with the fusion realized by Kalman filter. The novelty of our approach is the improvement of the RTS trajectory tracking system by combining the low-cost IMU sensor, even if the intervals between RTS measurements are longer. Our method can also overcome the problem of short (few seconds) RTS signal loss during the kinematic tracking process.

In the first part of our paper (Section 2), we describe the IMU calibration procedure needed for further experimental work. In Section 3,

our experimental work is explained, with used methods, results and analysis based on the comparison between reference trajectory, measured trajectory, and computed trajectory. The motion of the object was initiated using the flexible collaborative robotic arm UR5e and Quanser Shake Table. We measured trajectories with the MPU-9250 IMU sensor and Leica MS50, while the reference trajectories were measured with the Optotrak Certus and a Quanser Shake Table. The discussion and conclusions are presented in Section 4.

2. Sensor noise analysis and IMU calibration

2.1. IMU sensor noise analysis using Allan variance

For the experiment we used the low-cost multi-chip IMU module MPU-9250, consisting of a tri-axis accelerometer, tri-axis gyroscope, and tri-axis magnetometer. Each raw output signal of the IMU sensor contains the sum of the signal of interest (ideal signal) and the noise. Identification of the noise and its analysis leads us to information on how many samples of the output signal should be averaged in order to minimize the variance of the sensor output signal. The random noise parameters of the sensors are commonly characterized by the Allan variance. The procedure for calculating Allan variance is well described in [15–17].

We can read out the time needed for the sensor measurements to converge from the log-log plot of the overlapping Allan variance. The bias of the sensor should be averaged over this period of time, as the average bias will not change significantly over the next period. Within this period of time, the random process can be treated as white noise.

To define the period of time in which random processes could be treated as white noise, a sensor noise analysis was performed using the Allan variance. All measurements were performed at room temperature. The Allan deviation graphs for the gyroscope and accelerometer are shown in Fig. 1. The time needed for σ of the accelerometer and the gyroscope measurements to converge was about 20 s. This was taken into account when obtaining the IMU measurements for calibration. The static sensor signals during the calibration process were averaged over the determined time interval.

2.2. IMU calibration

Using 9-DoF IMU measurements, we can calculate the navigation parameters, which consist of the attitude, velocity, and position of the object in 3D space. The main drawback of determining reliable navigation parameters of an object using a low-cost IMU is its systematic errors. Without proper calibration, a low-cost IMU sensor cannot be used for further applications. In this section, we present the procedure for calibrating magnetometer, accelerometer, and gyroscope.

2.2.1. Magnetometer calibration

The magnetometer measures the constant geomagnetic field and the combined magnetic noise induced by nearby electro-magnetic devices, which causes systematic errors such as scale factor, non-orthogonality, and bias. We can classify those noises into two groups: Soft iron and hard iron distortions [18]. Hard iron distortion is the result of permanent magnet and magnetic hysteresis, while soft iron distortion is caused by the interaction of a ferromagnetic compound with an external field-induced magnetism. For the calibration model, we can use the fact that the magnetic flux density vector is constant in any orientation. If we rotate the sensor in 3D space, in a perturbation-free environment and without any systematic errors in magnetometer measurements, the output readings should describe a center-originated sphere with a radius of the magnitude of the earth's magnetic field. Due to all of the mentioned errors, magnetometer measurements will describe a 3D ellipsoid shifted from the center. The calibration parameters of a three-axis magnetometer are, in fact, transformation parameters that transform any ellipsoid into a center-originated sphere [19].

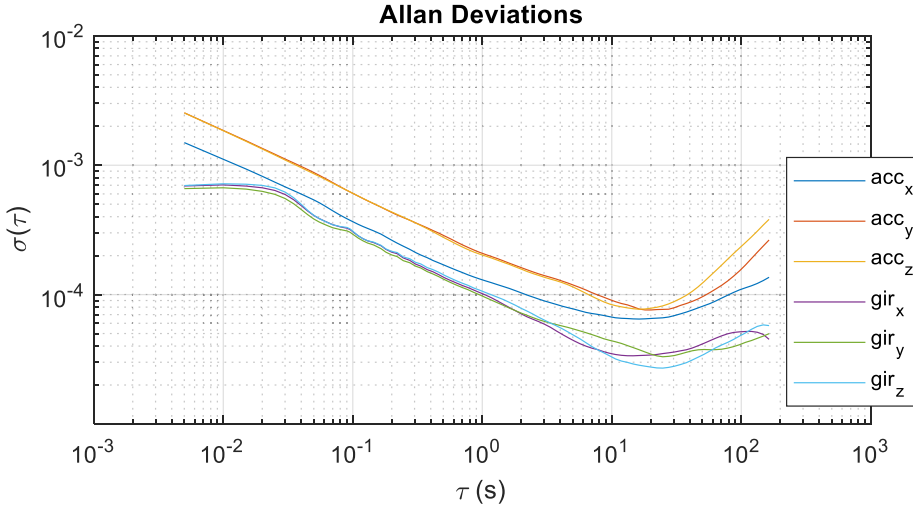


Fig. 1. Allan deviations for the gyroscope and accelerometer measurements of the IMU MPU9259.

A second-order algebraic surface is given by a general equation:

$$Ax^2 + By^2 + Cz^2 + 2Dxy + 2Exz + 2Fyz + 2Gx + 2Hy + 2Iz - 1 = 0 \quad (1)$$

where the constant parameter is already set to -1 . The general equation describes all types of quadratic surfaces. To describe an ellipsoid, proper constraints must be added [20]:

$$i = A + B + C, j = AB + BC + AC - F^2 - E^2 - D^2, 4j - i^2 > 0. \quad (2)$$

We can solve equation (1) by obtaining all nine parameters $[ABCDEFGHI]$ with the algebraic ellipsoid fitting method, which has been well-described in [20].

The calibration model of the magnetometer can be formed as [18]:

$$\mathbf{c} = \mathbf{T}(\mathbf{u} - \mathbf{b} - \boldsymbol{\epsilon}), \quad (3)$$

$$\mathbf{u} = [m_{ux} m_{uy} m_{uz}]^T \quad \mathbf{b} = [b_x b_y b_z]^T \quad \mathbf{T} = \begin{bmatrix} t_{11} & t_{12} & t_{13} \\ t_{21} & t_{22} & t_{23} \\ t_{31} & t_{32} & t_{33} \end{bmatrix}, \quad (4)$$

where \mathbf{c} is the error-free magnetic field in the sensor frame, \mathbf{u} is the vector of the raw readings from the tri-axis magnetometer, \mathbf{b} is the vector of the combined bias describing the hard iron disturbances, \mathbf{T} is the transformation matrix combining scale factors, misalignments, and soft iron disturbances, and $\boldsymbol{\epsilon}$ is the Gaussian wideband noise $\sim N(0, \sigma_e^2)$.

The combined bias \mathbf{b} represents the origin of the 3D ellipsoid, which is described by measurements of rotating sensor:

$$\mathbf{H}\mathbf{b} + \mathbf{g} = \mathbf{0}_{3\times 1} \quad (5)$$

where

$$\mathbf{H} = \begin{bmatrix} A & D & E \\ D & B & F \\ E & F & C \end{bmatrix}, \quad \mathbf{g} = [G \ H \ I]^T, \quad \mathbf{0}_{3\times 1} = [0 \ 0 \ 0]^T. \quad (6)$$

We can estimate the center of the 3D ellipsoid, $\mathbf{b} = [x_0 \ y_0 \ z_0]$, by [21]:

$$\mathbf{b} = -\mathbf{H}^{-1}\mathbf{g}. \quad (7)$$

The transformation matrix \mathbf{T} is calculated as [18,22]:

$$\mathbf{T} = \frac{1}{\sqrt{\mathbf{g}^T \mathbf{H}^{-1} \mathbf{g} - \mathbf{d}}} \mathbf{H}^{\frac{1}{2}}, \quad (8)$$

where \mathbf{d} is equal to a constant parameter (4): $\mathbf{d} = -1$.

2.2.2. Accelerometer calibration

The accelerometer can be calibrated using various approaches, such as the multi-position test [23], with the use of the low-cost 3 DoF robotic arm [24], the ellipsoid fitting method and others. Considering that the magnitude of the tri-axial accelerometer should be equal to the local gravity magnitude, we can use the same ellipsoid fitting calibration method as for the magnetometer, but the rotating sensor should not be under any other influence than the gravitational force.

In our case, we use the general form of least-squares adjustment [25]. The error model of the accelerometer can be expressed as [26,27]:

$$\mathbf{a}_b = \mathbf{T}\mathbf{u} - \mathbf{b}, \quad \mathbf{T} = \begin{bmatrix} k_{11} & 0 & 0 \\ k_{21} & k_{22} & 0 \\ k_{31} & k_{32} & k_{33} \end{bmatrix}, \quad (9)$$

where \mathbf{a}_b is the vector of the calibrated accelerometer readings $[a_x, a_y, a_z]^T$, \mathbf{T} is the transformation matrix including the scale factors (k_{11}, k_{22}, k_{33}), the off-diagonal sensitivity scale factors, and the misalignment elements (k_{21}, k_{31}, k_{33}), \mathbf{u} is the vector of the raw tri-axial readings $[a_{ux}, a_{uy}, a_{uz}]^T$, and \mathbf{b} is the vector of corresponding biases $[b_x, b_y, b_z]^T$.

The magnitude of the tri-axial accelerometer measurements in static state should be equal to the magnitude of local gravity \mathbf{g} . For the i^{th} reading, we can write:

$$g^2 = a_x^2 + a_y^2 + a_z^2 \quad (10)$$

The calibration parameters can be estimated by solving the following minimization problem:

$$F(\hat{\mathbf{T}}, \hat{\mathbf{b}}) = \operatorname{argmin} \sum_{i=1}^N \left(g^2 - (a_{xi}^2 + a_{yi}^2 + a_{zi}^2) \right), \quad (11)$$

where N is the number of static accelerometer placements. Using equations (9) and (11), we can write:

$$F_i = g^2 - (k_{11}a_{uxi} - b_x)^2 - (k_{21}a_{uyi} + k_{22}a_{uyi} - b_y)^2 - (k_{31}a_{uzi} + k_{32}a_{uyi} + k_{33}a_{uzi} - b_z)^2, \quad (12)$$

where a_{uxi}, a_{uyi} , and a_{uzi} are the averages of raw accelerometer readings obtained from the i^{th} orientation.

Using the general form of the least-squares adjustment model, we can write:

$$\mathbf{A}(\mathbf{l} + \mathbf{v}) + \mathbf{B}\Delta = \mathbf{d}, \quad (13)$$

where \mathbf{A} and \mathbf{B} are the coefficient matrices, \mathbf{d} is the column vector of constants, \mathbf{l} is the vector of sample values of the observational variables, and \mathbf{v} is the vector of residuals.

We can substitute $\mathbf{f} = \mathbf{d} - \mathbf{Al}$ and form:

$$\mathbf{Av} + \mathbf{B}\Delta = \mathbf{f}. \quad (14)$$

In our case, \mathbf{A} is a block-diagonal matrix, where the i^{th} element of the matrix \mathbf{A} is:

$$\mathbf{A}_i = \text{diag} \left(\begin{bmatrix} \frac{\partial F_i}{\partial a_{ux}} & \frac{\partial F_i}{\partial a_{uy}} & \frac{\partial F_i}{\partial a_{uz}} \end{bmatrix} \right) \mathbf{A} = \begin{bmatrix} \mathbf{A}_1 & \cdots & 0 \\ \vdots & \ddots & \vdots \\ 0 & \cdots & \mathbf{A}_N \end{bmatrix}, \quad (15)$$

the i^{th} row of the design matrix \mathbf{B} is:

$$\mathbf{B}_i = \begin{bmatrix} \frac{\partial F_i}{\partial b_x} & \frac{\partial F_i}{\partial b_y} & \frac{\partial F_i}{\partial b_z} & \frac{\partial F_i}{\partial k_{11}} & \frac{\partial F_i}{\partial k_{22}} & \frac{\partial F_i}{\partial k_{33}} & \frac{\partial F_i}{\partial k_{21}} & \frac{\partial F_i}{\partial k_{31}} & \frac{\partial F_i}{\partial k_{32}} \end{bmatrix} \mathbf{B} = [\mathbf{B}_1 \ \cdots \ \mathbf{B}_N]^T \quad (16)$$

and the i^{th} element of the vector \mathbf{f} is:

$$\mathbf{f}_i = (k_{11}a_{uxi} - b_x)^2 + (k_{21}a_{uxi} + k_{22}a_{uyi} - b_y)^2 + (k_{31}a_{uxi} + k_{32}a_{uyi} + k_{33}a_{uzi} - b_z)^2 - g^2 \quad (17)$$

$$\mathbf{f} = [\mathbf{f}_1 \ \cdots \ \mathbf{f}_N]^T.$$

The unknown parameters Δ are, in our case, the corrections of estimated calibration parameters:

$$\Delta = [\delta b_x \ \delta b_y \ \delta b_z \ \delta k_{11} \ \delta k_{22} \ \delta k_{33} \ \delta k_{21} \ \delta k_{31} \ \delta k_{32}]^T \quad (18)$$

The vector Δ can be obtained as [25]:

$$\Delta = (\mathbf{B}^T(\mathbf{A}\mathbf{Q}\mathbf{A}^T)^{-1}\mathbf{B})^{-1}\mathbf{B}^T(\mathbf{A}\mathbf{Q}\mathbf{A}^T)^{-1}\mathbf{f}, \quad (19)$$

where \mathbf{Q} is the cofactor matrix of the observations. If the observations (in our case, accelerometer measurements) have the same accuracy, \mathbf{Q} is the unit matrix.

At the first iteration of the adjustment, we can set the estimated values of the calibration parameters as:

$$\mathbf{T}_0 = \begin{bmatrix} 1 & 0 & 0 \\ 0 & 1 & 0 \\ 0 & 0 & 1 \end{bmatrix}, \quad \mathbf{b}_0 = [0 \ 0 \ 0]^T. \quad (20)$$

Iterations of the adjustment run as long as $|\Delta| > \epsilon$, where ϵ is an arbitrarily chosen small number.

2.2.3. Gyroscope calibration

Gyroscopes can be calibrated in various ways. The bias of the gyroscope can be determined simply by averaging the readings at a static

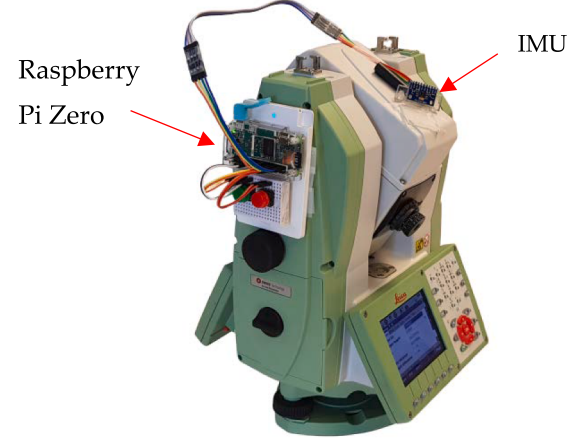


Fig. 2. IMU calibration with Leica Nova MS50.

position. For the determination of other calibration parameters, we have to take a different approach. Some methods require turn-tables which provide an exact angular rate [28], while others combine the gyroscope with other IMU sensors (i.e., accelerometer and/or magnetometer) [26,29,30]. We calibrated the gyroscope in the angle domain using a robotic total station Leica Nova MS50 as a single-axis turn-table, providing an exactly chosen angular rotation. We mounted the IMU on the RTS (Fig. 2) three times at different orientations and rotated it around fixed axis multiple times at a known arbitrary chosen angle using the GeoCOM protocol [31].

Since the axis of rotation is constant during the measurement interval the integrated angle rates should be equal to the known i^{th} angle of rotation α_i [32]:

$$\omega_i^2 = \sum_{j=1}^M \left((\omega_{x_{j_i}}^2 + \omega_{y_{j_i}}^2 + \omega_{z_{j_i}}^2) \Delta t_{j_i}^2 \right), \quad (21)$$

where M is the number of gyroscope readings in the i^{th} rotation of RTS, and $\omega_{x_{j_i}}, \omega_{y_{j_i}}$, and $\omega_{z_{j_i}}$ are calibrated gyroscope readings. The procedure of the gyroscope calibration model and the calculation of the calibration parameters is consistent with the accelerometer's model given by Eq. (9) [17].

2.2.4. Results of IMU calibration

All calibrations and experimental measurements were performed at

Table 1
The MPU9250 calibration parameters.

	T	b
Accelerometer	$T = \begin{bmatrix} 1.016258 & 0 & 0 \\ 0.001235 & 1.017346 & 0 \\ -0.000385 & -0.004319 & 1.026368 \end{bmatrix}$	$b = \begin{bmatrix} -0.008621 \\ -0.010693 \\ 0.041037 \end{bmatrix} \text{ m/s}^2$
Gyroscope	$T = \begin{bmatrix} 0.95875 & 0 & 0 \\ 0.00083 & 0.94062 & 0 \\ -0.00023 & 0.00306 & 0.95513 \end{bmatrix}$	$b = \begin{bmatrix} -0.03 \\ 0.02 \\ -0.11 \end{bmatrix} \text{ mrad/s}$
Magnetometer	$T = \begin{bmatrix} 1.2203 & 0.0222 & -0.0225 \\ 0.0222 & 1.1740 & 0.0656 \\ -0.0225 & 0.0656 & 1.2098 \end{bmatrix}$	$b = \begin{bmatrix} 3.30 \\ 38.86 \\ -16.52 \end{bmatrix} \mu\text{T}$

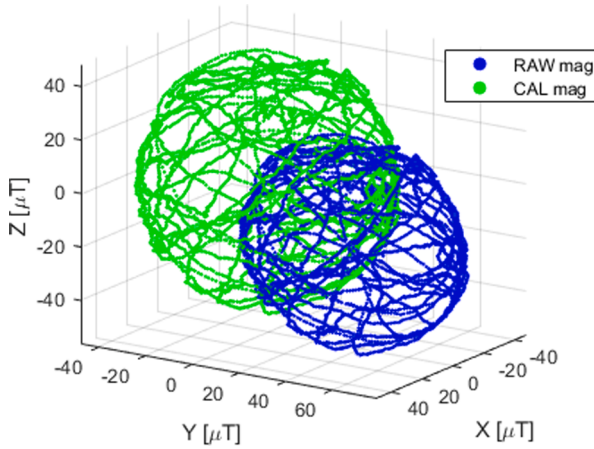


Fig. 3. Magnetometer calibration.

room temperature. The influence of temperature variations on the IMU calibration parameters was not considered, as it is outside the scope of this paper. The calibration parameters of our IMU MPU9250 are listed in Table 1. A graphical representation of the magnetometer calibration is shown in Fig. 3. The blue and green colors represent raw and calibrated magnetometer readings, respectively.

2.3. Calculation of navigation parameters

Using the calibrated IMU measurements, we can describe the object in 3D space, in terms of its current attitude, velocity, and position. Definition of coordinate frames used in navigation applications and step by step computation of navigation parameters from IMU measurements in local-level frame are well described in [33].

3. Experimental work

We conducted two experiments. The aim of the first experiment was to evaluate the quality of standalone low-cost IMU positioning using ZPF. In the second experiment, we performed a geodetic, highly dynamic, continuously tracking kinematic survey of an instructional shake table during earthquake simulation. The aim of the second experiment was to explore the possibility of increasing the accuracy of geodetic RTS kinematic measurements by combining low-cost IMU measurements.

3.1. Experiment 1: Quality evaluation of standalone low-cost IMU positioning with the use of ZPF

With this experiment, we aimed to evaluate the accuracy of low-cost IMU positioning of oscillating objects. Since the high-pass ZPF procedure eliminates any permanent and low-frequency displacement, we induced an oscillating movement exactly around the zero point. With this approach, we can evaluate the accuracy of the trajectory measured with a low-cost IMU and processed with the ZPF procedure by direct comparison with the reference trajectory.

For the experiment we used the low-cost multi-chip IMU module MPU-9250, consisting of a tri-axis accelerometer, tri-axis gyroscope, and tri-axis magnetometer. We induced oscillating movements around the zero-point with an UR5e flexible collaborative robotic arm equipped with a Hand-E adaptive robotic gripper. The trajectory measured by the calibrated low-cost IMU and processed with the ZPF was compared with the reference trajectory measured by the Optotak Certus® motion capture system, with a nominal accuracy of 0.1 mm. We used a Leica Nova Multistation MS50 for measuring the control points required to determine the transformation between the IMU body frame coordinate system and the Optotak local coordinate system. The RTS angle measurement accuracy was $\sigma_{ISO-THEO-HZ,V} = 1''$ and the distance measurement accuracy was $\sigma_{ISO-EDM} = 1\text{mm}; 1\text{ppm}$.

3.1.1. Experimental measurements

The experiment was conducted in the Laboratory of robotics, University of Ljubljana, Faculty of Electrical Engineering. The experimental setup is shown in Fig. 4. The robotic arm induced a movement in 3D space around the zero point, while the reference trajectory was

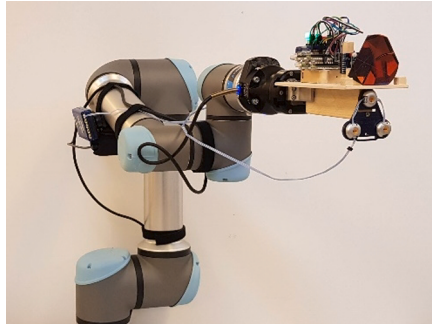


Fig. 5. Robotic arm with IMU module.

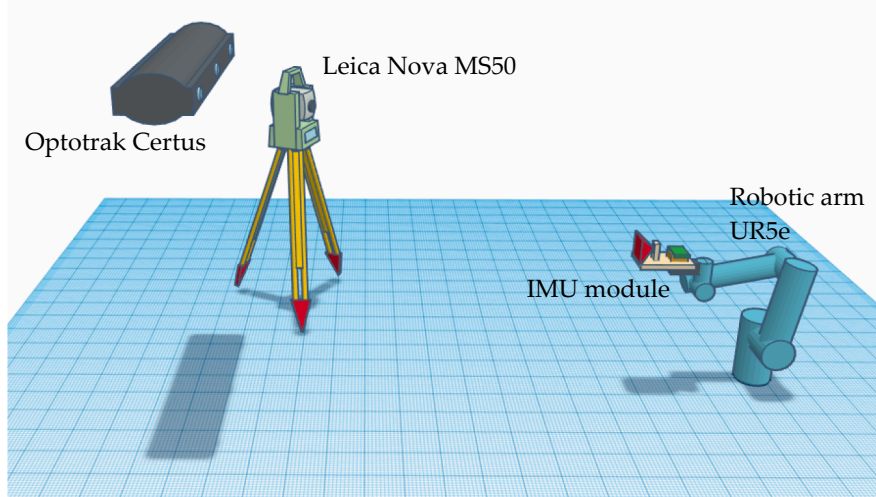


Fig. 4. Experimental setup.

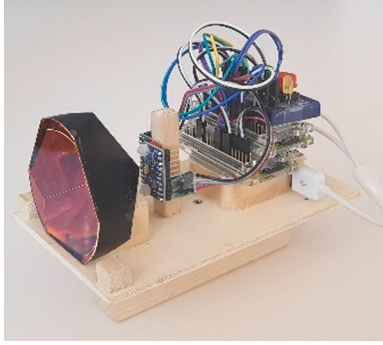


Fig. 6. IMU module.



Fig. 7. Optotak Certus and Leica MS50.

measured by the Optotak at 400 Hz. Infrared markers were placed on the IMU module, as shown in Fig. 5. IMU measurements were recorded at 200 Hz. The IMU module is shown in Fig. 6. The IMU module was a combination of the IMU sensor MPU-9250, a Raspberry Pi Zero with a 1 GHz single-core CPU and 512 Mb RAM, and the Leica prism, which was needed to determine the initial position of the IMU sensor. The Leica MS50 and Optotak are shown in Fig. 7.

3.1.2. Reference trajectory

The trajectory of the object measured by the Optotak was the reference against which the processed IMU trajectory was compared. The trajectory of the IMU module measured by the Optotak is shown in Fig. 8. All results are presented in the local coordinate system, with the origin at the initial position of the IMU module, the z-axis of coordinate system pointing upwards, and the orientation of the x-axis and y-axis chosen arbitrarily. Time synchronization of the systems was performed by cross-correlation of the IMU and Optotak signals. The movement procedure of the IMU module around the zero point took about 60 s and is presented in Video 1 in the Appendix.

3.1.3. IMU trajectory

Any uncompensated error of the accelerometer and/or gyroscope would induce an inaccuracy, which is reflected in the calculated object attitude, velocity, and position. Sources for such errors are noise, scale-factor errors, and bias errors. The biggest effect is the bias error, which consists of two parts: the short-term deterministic offset and the long-term random drift (bias instability) [33,34]. These errors are reflected in low-frequency position drift. For this reason, a low-cost IMU is not suitable for stand-alone use in determining an object's position without further processing.

3.1.3.1. Zero-phase filter. Using a high-pass filter, we could retain information about the actual movement of the object. In real-time applications, we must use causal filters, which introduce a phase shift. As we are dealing with an off-line application of a position monitoring system, we could use Zero-Phase Filtering with an IIR filter, which is a non-causal filter with zero phase shift.

The Zero-Phase filter is a special case of the linear-phase filter, which delay all frequencies by the same amount, thus maximally preserving waveshape [35]. Zero-Phase filter uses the time-reversal property of the discrete-time Fourier transform [36]:

$$x[n] \leftrightarrow {}^{DTFT}X(e^{j\omega T}) \Leftrightarrow x[-n] \leftrightarrow {}^{DTFT}X^*(e^{j\omega T}), \quad (22)$$

where the finite input signal is $x[n]$ and $h[n]$ is the filter's impulse response. In the Fourier domain, we can write:

$$Z(e^{j\omega T}) = X(e^{j\omega T})H(e^{j\omega T}) \quad (23)$$

The use of the time-reverse property leads us to:

$$W(e^{j\omega T}) = Z^*(e^{j\omega T}) = X^*(e^{j\omega T})H^*(e^{j\omega T}) \quad (24)$$

Then, we use $H(e^{j\omega T})$ again:

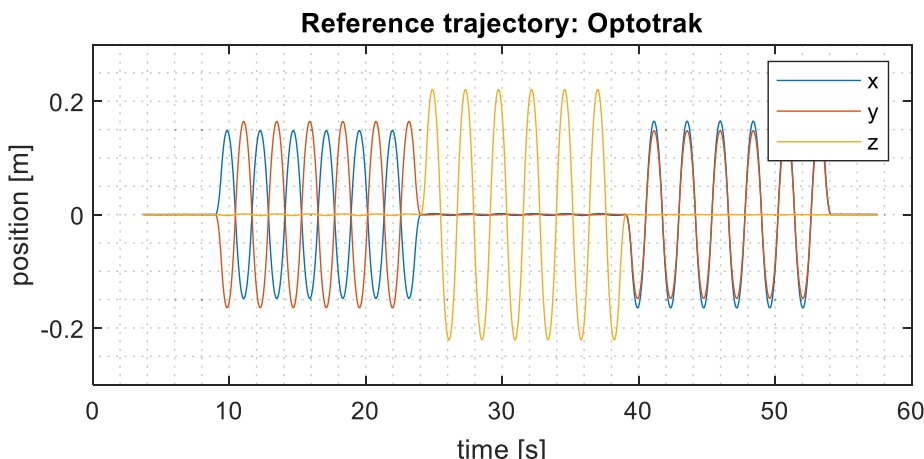


Fig. 8. Reference trajectory.

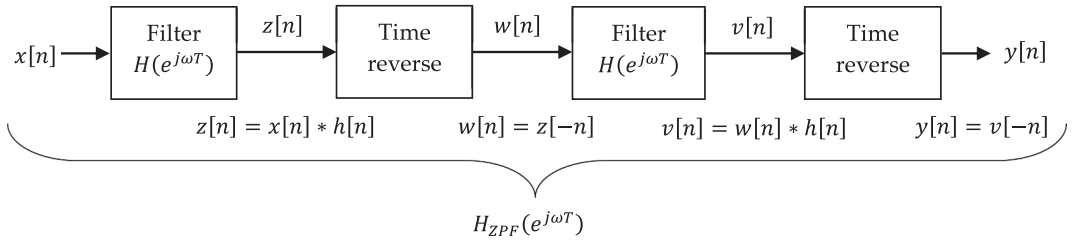


Fig. 9. Flowchart of the Zero-Phase filter procedure.

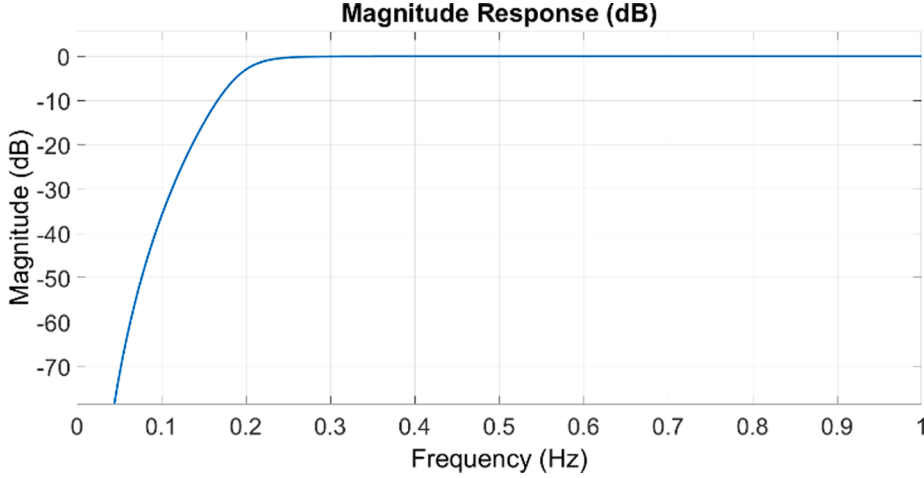


Fig. 10. Magnitude response of the Zero-phase filter $H_{ZPF}(e^{j\omega T})$ function.

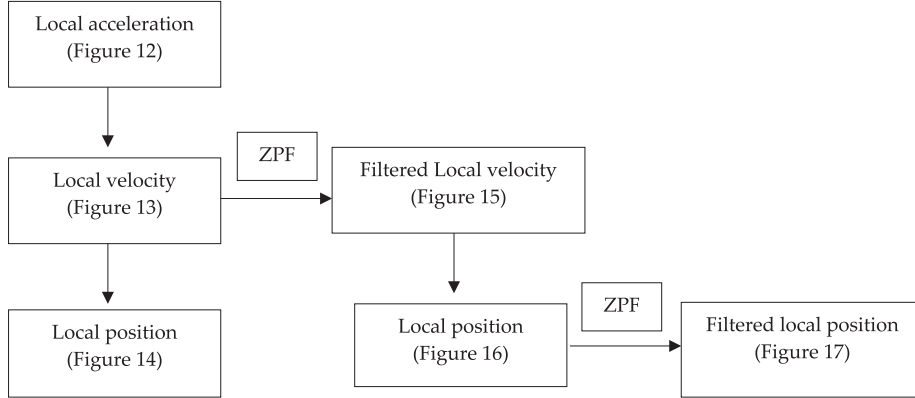


Fig. 11. Diagram of the calculation steps.

$$\begin{aligned} V(e^{j\omega T}) &= Z^*(e^{j\omega T})H(e^{j\omega T}) = X^*(e^{j\omega T})H^*(e^{j\omega T})H(e^{j\omega T}) \\ &= X^*(e^{j\omega T})|H(e^{j\omega T})|^2. \end{aligned} \quad (25)$$

After performing another time-reverse, we get:

$$Y(e^{j\omega T}) = V^*(e^{j\omega T}) = X(e^{j\omega T})|H(e^{j\omega T})|^2, H_{ZPF}(e^{j\omega T}) = |H(e^{j\omega T})|^2. \quad (26)$$

After double filtering, we get an output signal with zero phase shift. The frequency components of the input signal are multiplied by $|H(e^{j\omega T})|^2$. The overall filter function $H_{ZPF}(e^{j\omega T})$ is real and positive [36,37]. A schematic representation of the procedure of the Zero-phase filter $H_{ZPF}(e^{j\omega T})$, based on Eqs. (22)–(26), is shown in the flowchart in Fig. 9 [38]. Fig. 10 gives the example of the magnitude response of the Zero-phase filter.

3.1.3.2. Final IMU trajectory. The diagram of the process steps to achieve the final high-pass filtered IMU trajectory is shown in Fig. 11. Using the calibrated IMU measurements, we calculated the acceleration, velocity, and position of the body in the Local Level Frame which are shown in Figs. 12, 13, and 14, respectively. We can see an enormous drift of the local velocity (Fig. 13), about 15 m/s in 60 s, and a drift of the local position (Fig. 14), about 500 m in 60 s. To obtain the final high-pass filtered trajectory, we designed a sixth-order Butterworth filter with a cutoff frequency at 0.2 Hz and a Zero-phase filter. The Zero Phase Filter was implemented, in MATLAB®, as the *filtfilt* function. First, we applied the ZPF to the local velocity of the object in the Local Level Frame (Fig. 13) and obtained the filtered local velocity (Fig. 15), in which the low-frequency velocity drift was eliminated. Based on the filtered local velocity, we calculated the position (Fig. 16), which served as the input to the last step of the filtering. The final filtered trajectory is

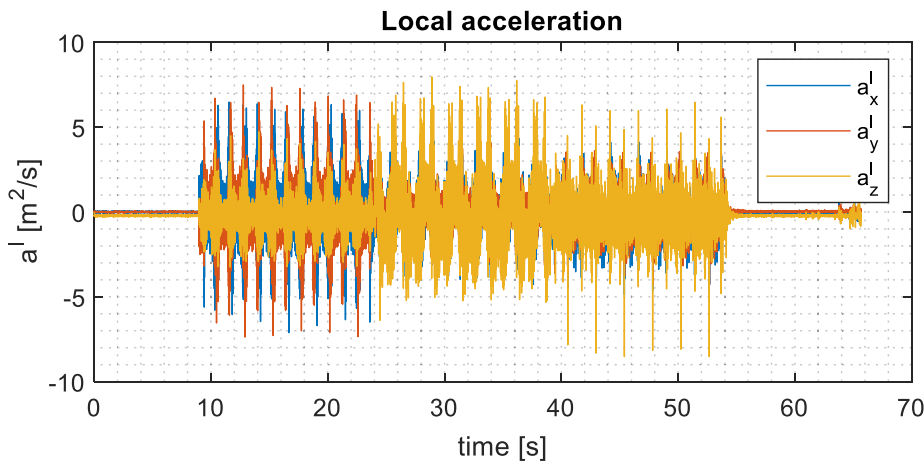


Fig. 12. The body acceleration in the Local Level Frame.

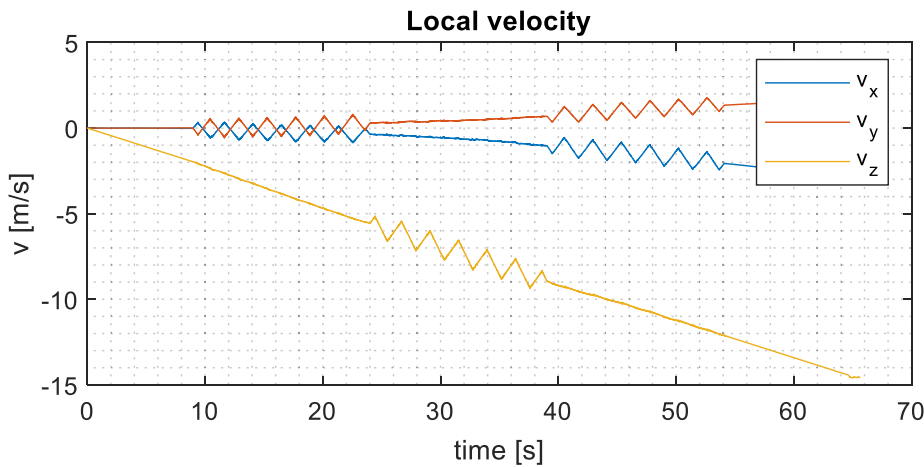


Fig. 13. The velocity in the Local Level Frame.

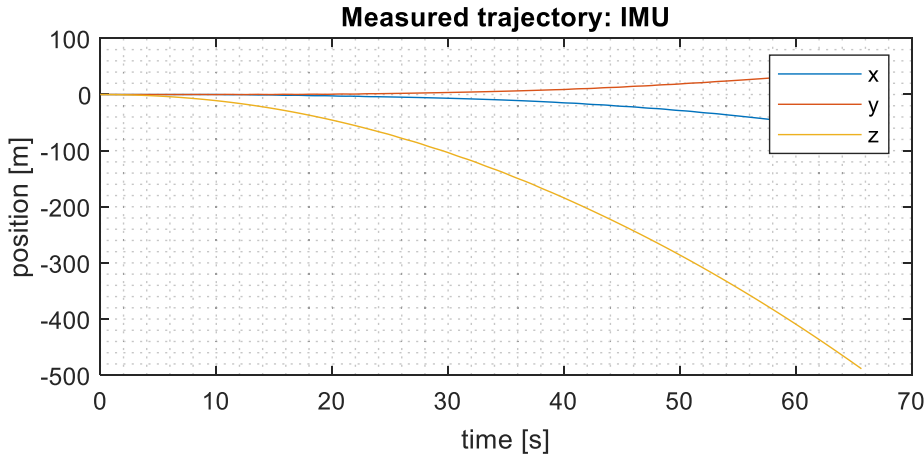


Fig. 14. The trajectory in the Local Level Frame.

shown in Fig. 17.

The quality of the IMU measurements and the proposed filtering procedure were estimated by comparing the reference trajectory (Fig. 8) and the final filtered trajectory of the IMU module (Fig. 17) for each axis in the Local Level Frame, as shown in Fig. 18. In Fig. 19, the difference between the reference trajectory and the final filtered trajectory is shown. The animation of the reference and final filtered trajectory

beside the actual movement of the IMU module is shown in Video 1 in the Appendix.

We can see, from Fig. 19, that the differences between the trajectories were within a few centimeters. We defined three quality estimators of the final filtered IMU trajectory: The first was the root-mean-square error of the filtered (Fig. 17) and reference (Fig. 8) trajectories, the second was the Signal-to-noise ratio, and the third one was the

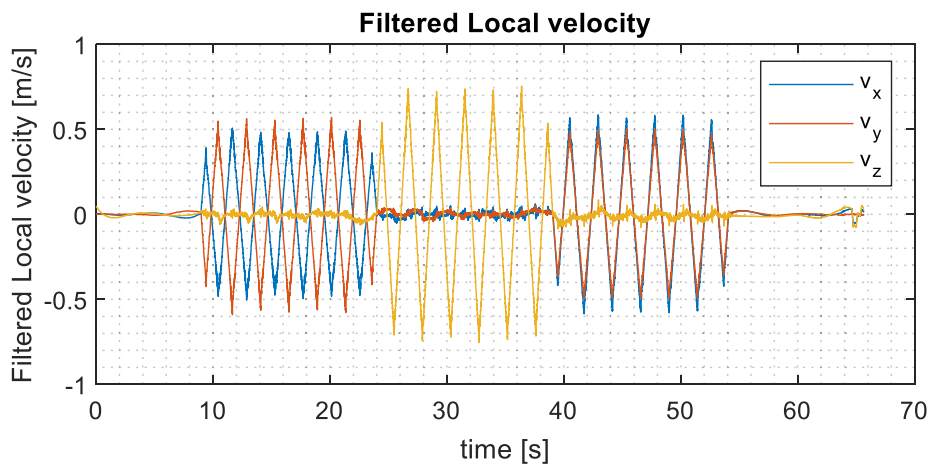


Fig. 15. The filtered local velocity.

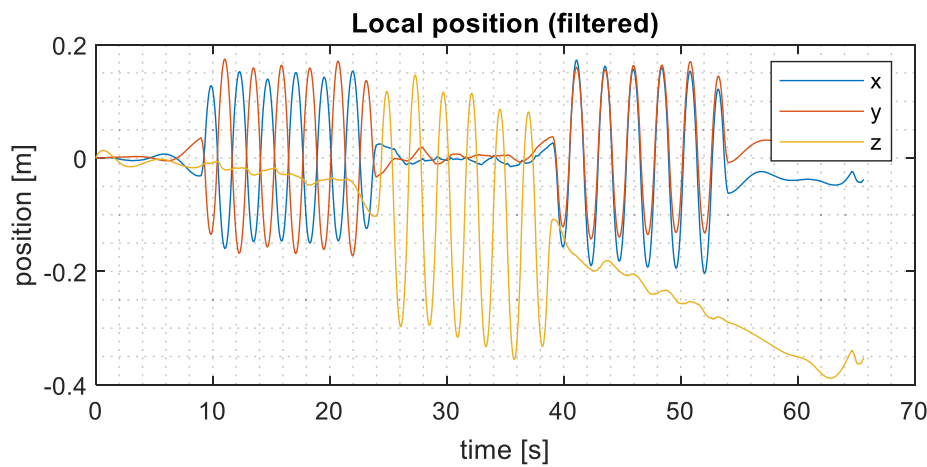


Fig. 16. The trajectory in the Local Level Frame (calculated from the filtered local velocity).

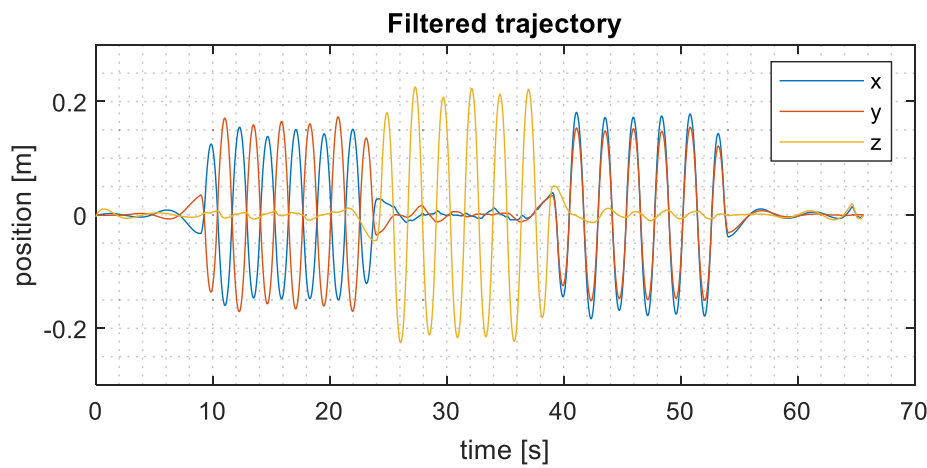


Fig. 17. The final filtered trajectory.

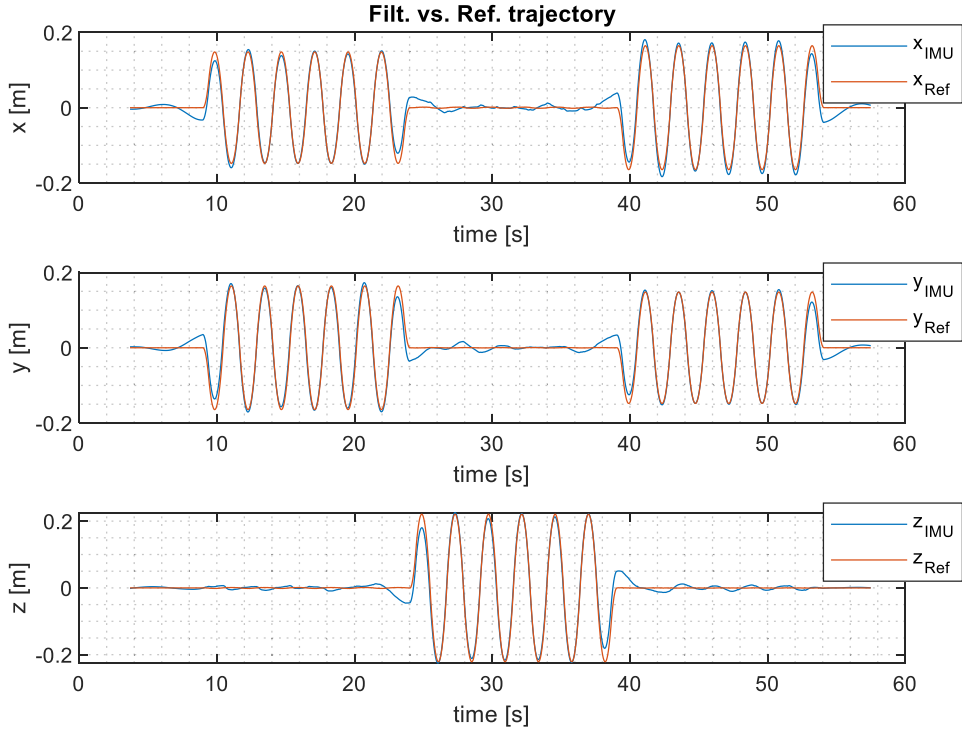


Fig. 18. Comparison of the reference trajectory and the filtered trajectory.

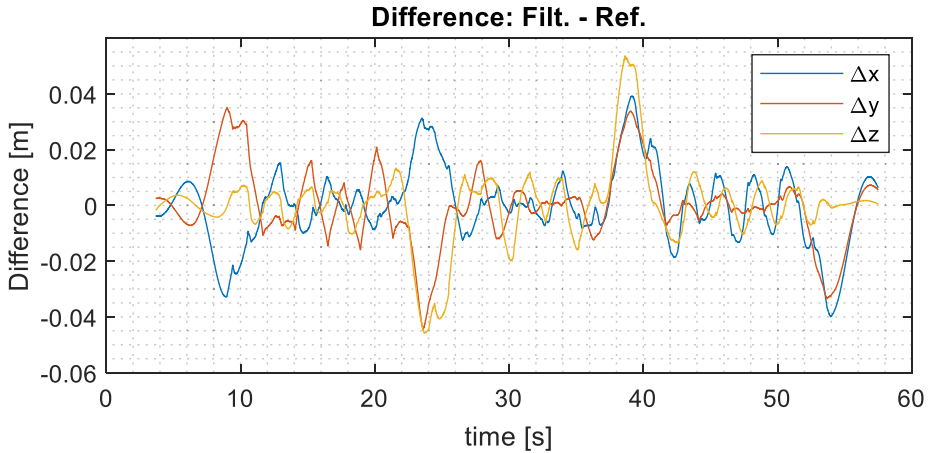


Fig. 19. Difference between the filtered trajectory and the reference trajectory.

correlation of the filtered and the reference trajectories.

The root-mean-square error between the trajectories ($RMSE_r$) was calculated as:

$$RMSE_r = \sqrt{\frac{\sum_{i=1}^n (r_{IMU_i} - r_{Ref_i})^2}{n}}, \quad (27)$$

where r_{IMU} and r_{Ref} are the coordinates of the trajectories obtained by the IMU measurements and Optotrak measurements, respectively and n is sample size of the signals.

The signal-to-noise ratio (SNR) was calculated as:

$$SNR = \left(\frac{A_{signal}}{A_{noise}} \right)^2, \quad (28)$$

where A_{signal} is the root-mean-square of the signal (in our case, filtered trajectory) and A_{noise} is the root-mean-square of the noise (in our case, the difference between filtered and reference trajectory). The SNR

can be expressed, in decibels, as:

$$SNR_{dB} = 10\log_{10}(SNR). \quad (29)$$

The correlation between two signals r_{IMU} and r_{Ref} is calculated as:

$$corr = \frac{1}{n-1} \sum_{i=1}^n \left(\frac{r_{IMU_i} - \bar{r}_{IMU}}{std(r_{IMU})} \right) \left(\frac{r_{Ref_i} - \bar{r}_{Ref}}{std(r_{Ref})} \right), \quad (30)$$

where n is sample size of the signals r_{IMU} and r_{Ref} .

The quality estimators for the first experiment were:

$$RMSE_r = 2.4\text{cm}$$

$$SNR = 36.7$$

$$SNR_{dB} = 15.6\text{dB},$$

$$corr = 0.987$$

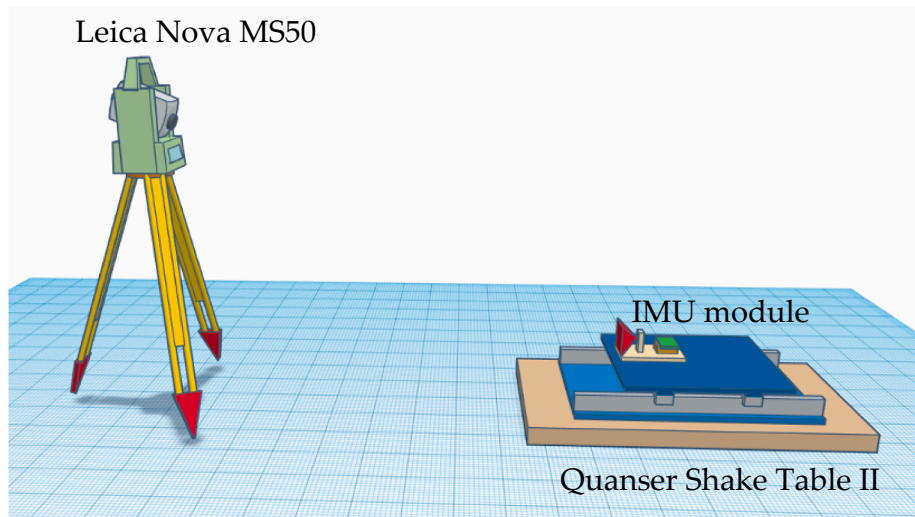


Fig. 20. The second experimental setup.

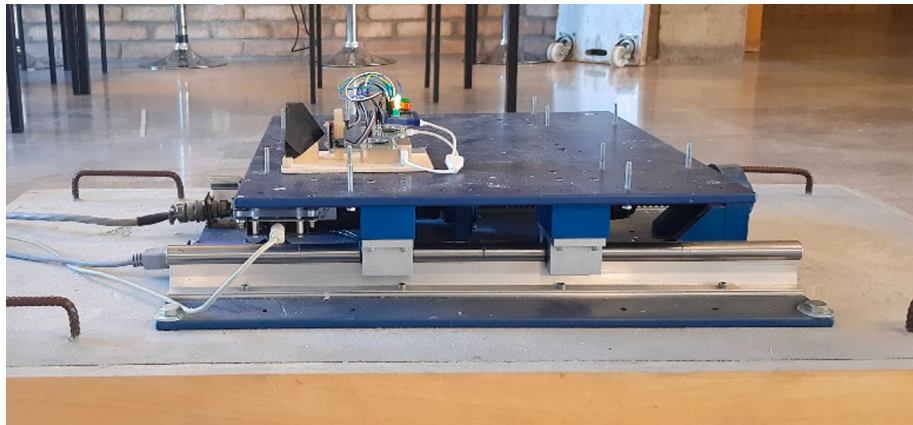


Fig. 21. Quanser Shake Table II and the IMU module.

After using a low-cost IMU as a standalone sensor for object positioning without further processing, we obtained a drift of 500 m after 60 s of measurement time. After the second ZPF step, we got usable results. The filtered trajectory coincided with the reference trajectory very well. The root-mean-square error between both trajectories was 2.4 cm. This deviation consists of a combination of errors resulting from the accuracy of the IMU sensor and the filtering procedure. Signal-to-noise ratio and the correlation of the filtered and the reference trajectories were 36.7

and 0.987 respectively.

3.2. Experiment 2: Continuous kinematic tracking survey with combination of low-cost IMU measurements

In the second experiment, we carried out a geodetic highly dynamic, continuously tracking kinematic survey of an instructional shake-table during earthquake simulation. We used the Quanser Shake Table II to

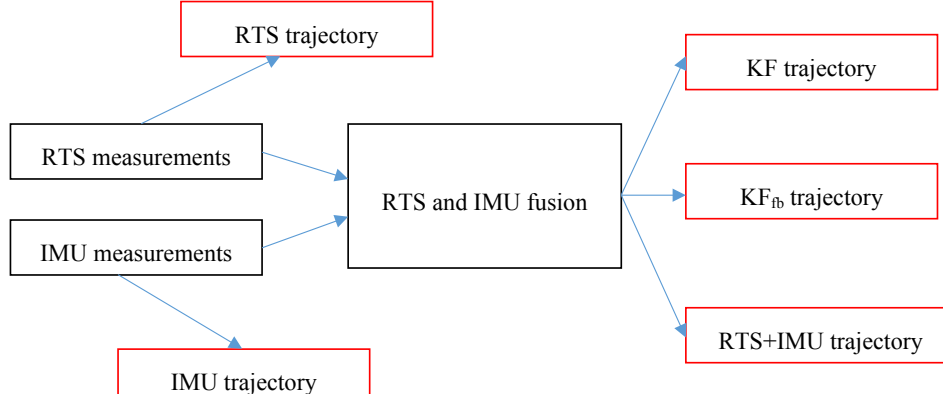


Fig. 22. Workflow diagram of Experiment 2.

simulate an earthquake, the robotic total station (RTS) Leica Nova MS50 for kinematic measurements using ATR (Automatic Target Recognition) technology, and low-cost IMU measurements as a supplement for the geodetic kinematic measurements. The aim of the experiment was to explore the possibility of increasing the accuracy of geodetic RTS kinematic measurements by combining low-cost IMU measurements. The reference trajectory was obtained by the Quanser Shake Table II.

3.2.1. Experimental measurements

The experiment was conducted at the Faculty of Civil and Geodetic Engineering of the University of Ljubljana. The experimental setup is shown in Fig. 20. The Quanser Shake Table II induced simulation of the earthquake movement while the IMU module (Fig. 6) was measured with the Leica MS50 using ATR and continuous tracking mode. The Leica MS50 was placed approximately in the direction of the shake-table movement. The MPU9250 measurements were recorded at 200 Hz, while the reference trajectory from the shake table had a resolution of 142 Hz. The IMU module and Quanser Shake Table II are shown in Fig. 21.

3.2.2. Results and analysis

In Experiment 2, we calculate and analyze different trajectories. From RTS and IMU measurements we calculated RTS and IMU trajectory, from RTS and IMU fusion, we calculated KF trajectory, KF_{fb} trajectory, and RTS + IMU trajectory (Fig. 22). Their explanation is found below.

3.2.2.1. RTS trajectory. The RTS was configured for automatic kinematic measurements with the highest frequency of 10 Hz, but the actual sampling time differed from the configuration. The RTS performed the measurements with an average sampling time of 0.15 s (~7 Hz). Inconsistencies in the time delay of RTS kinematic measurements of angle and distances are not discussed here, as they are outside the scope of this

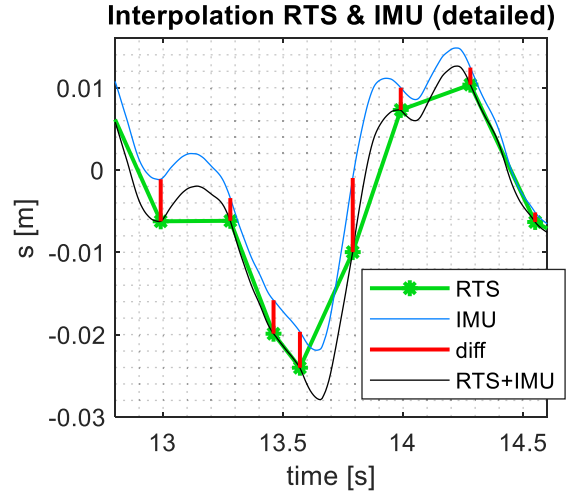


Fig. 24. Combined RTS and IMU trajectories.

paper. According to Nyquist's sampling theorem, we could correctly detect object motion if the frequency of the RTS measurement would be at least two times higher than the frequency of the object oscillation [39]. As the frequency of the RTS measurements is too low to describe movement of the instructional shake table representative, the RTS trajectory is presented by linear interpolation between the measured RTS points. In this case, any kinematic model applied to RTS points would lead to false representation of the trajectory movement.

3.2.2.2. IMU trajectory. For Experiment 2, we used the same IMU module as in Experiment 1. At this point, we have assumed that the calibration parameters (except gyroscope bias) have not changed significantly in the short time between the two experiments. The

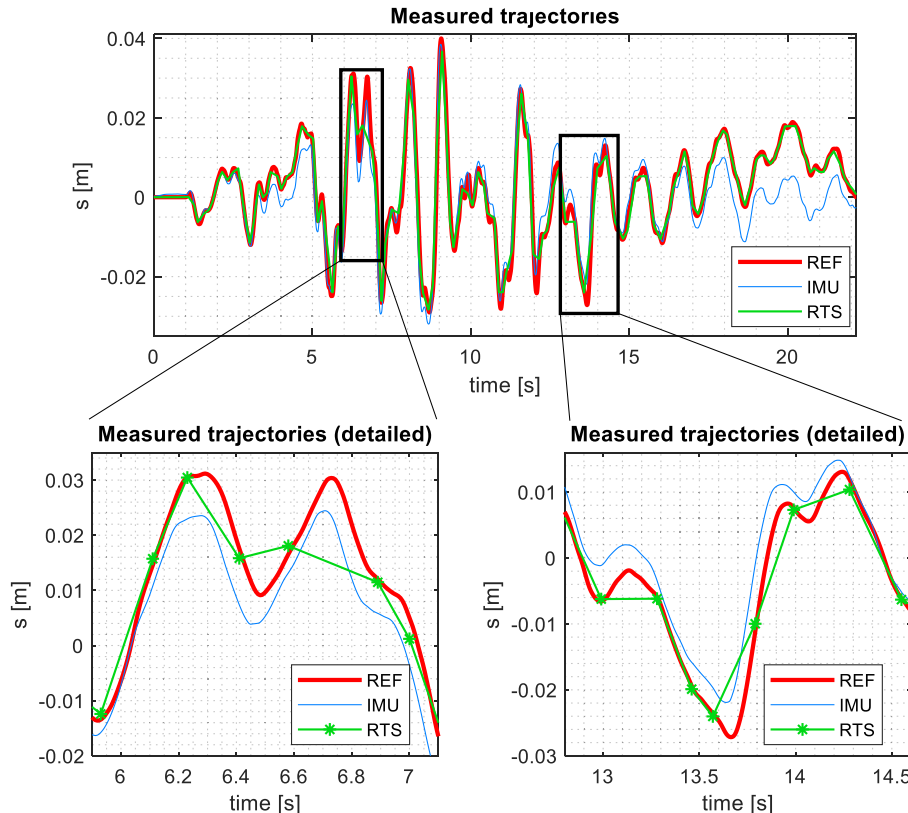


Fig. 23. Reference, RTS, and IMU trajectory.

gyroscope bias was redetermined at every IMU power-up. The study of IMU run-to-run random errors is beyond the scope of this paper. Nevertheless, the following results show that we have obtained good and reliable results using the IMU measurements calibrated with the same parameters. The IMU measurements were processed with the same ZPF procedure described in Experiment 1 (Fig. 11). Fig. 23 shows the reference trajectory, the RTS trajectory, and the IMU trajectory. As we can see in the detailed section of Fig. 23, the RTS points lay close to the reference trajectory but did not describe the actual trajectory movement well, due to the low frequency of the RTS measurement. The processed IMU trajectory described the relative waveform of the trajectory movement well. However, it was not positionally accurate, as the simulated earthquake movement did not oscillate exactly around the zero point, which is particularly evident in the sector around 20 s into the test.

3.2.2.3. RTS + IMU trajectory. The IMU and the RTS trajectories were combined using linear interpolation of the differences between both trajectories. The interpolated differences were then added to the IMU trajectory. We assumed that the points of the RTS trajectory were accurate in position and time. Interpolated differences were added to the RTS trajectory, as shown in Fig. 24, resulting in a combined trajectory (RTS + IMU).

3.2.2.4. KF trajectory. The fusion of high-frequency IMU measurements and low-frequency RTS measurements can also be performed using the multi-rate Kalman filter (KF) [13,14], which is the recursive optimal filter. The discrete-time application of KF requires that the system model and the observational model of the underlying process have to be linear. A discrete-time linear system model is described by the equation:

$$\mathbf{x}_{k+1} = \phi_{k+1} \mathbf{x}_k + \mathbf{G}_k \mathbf{w}_k \quad (31)$$

where \mathbf{x}_k is the state vector, ϕ_k is the state transition matrix, \mathbf{G}_k is the noise distribution matrix, and \mathbf{w}_k is the process noise vector.

In our case, the state vector is defined as $\mathbf{x}_k = [x^k \ v_x^k \ a_x^k]^T$, where x^k , v_x^k , a_x^k are the displacement, velocity, and acceleration of the object at the epoch k respectively. The state transition matrix ϕ_k is calculated from the dynamic model of the system:

$$\phi_k = \begin{bmatrix} 1 & \Delta t & \frac{\Delta t^2}{2} \\ 0 & 1 & \Delta t \\ 0 & 0 & 1 \end{bmatrix} \quad (32)$$

where Δt is the sampling period.

Observation model of Kalman filter describes connection between system model and observations. The discrete-time linear observation equation of the system is defined as:

$$\mathbf{z}_k = \mathbf{H}_k \mathbf{x}_k + \eta_k \quad (33)$$

where \mathbf{z}_k is the observation vector, \mathbf{H}_k is the design matrix, and η_k is the observation noise vector. Since the RTS and IMU measurements are taken with different sampling frequencies (7 Hz and 200 Hz

Table 2
The quality estimators of IMU, RTS, RTS*, KF, RTS + IMU, and KF_{fb}.

	IMU	RTS*	RTS	KF	RTS + IMU	KF _{fb}
RMSE _r	5.2 mm	1.6 mm	2.5 mm	4.9 mm	1.5 mm	1.3 mm
SNR	3.8	61.4	19.5	5.9	64.8	83.5
SNR _{dB}	5.7 dB	17.9 dB	12.9 dB	7.7 dB	18.1 dB	19.2 dB
corr	0.904	0.992	0.980	0.964	0.993	0.994

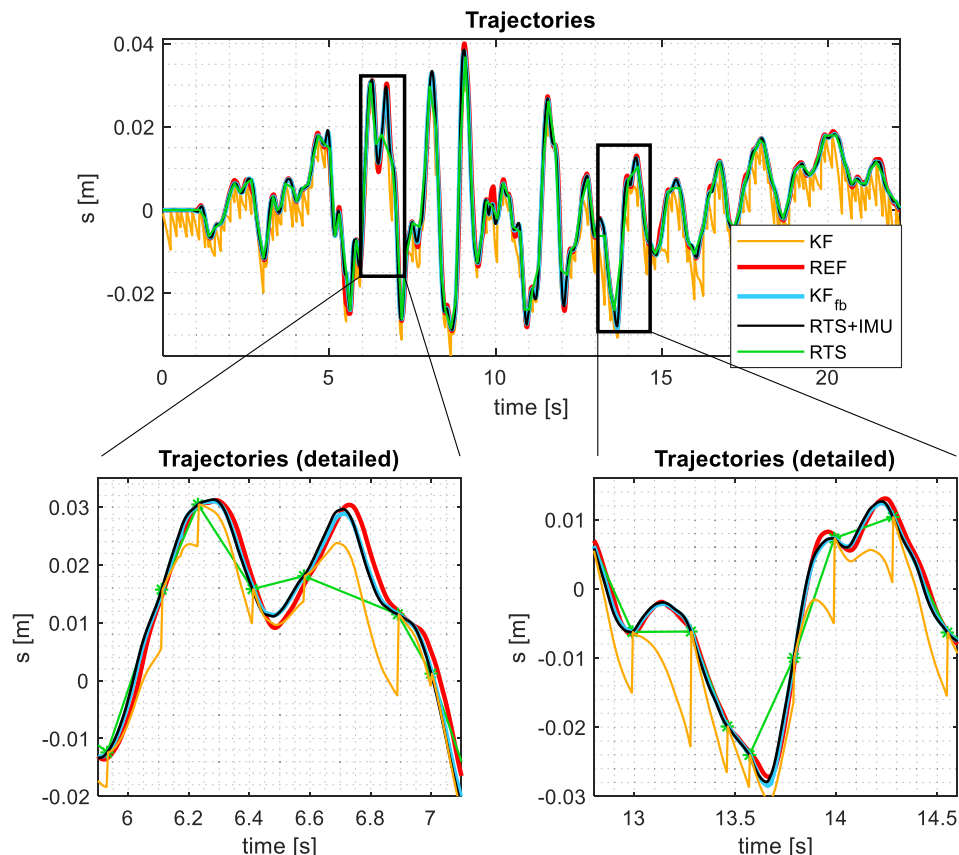


Fig. 25. Reference, KF, KF_{fb}, RTS + IMU, and RTS trajectories.

Table 3The quality estimators of RTS, KF_{fb}, and RTS + IMU trajectories.

$\bar{\Delta t}_{RTS}$	RMSE _r [mm]			SNR			corr		
	0.15 s	1.5 s	5.0 s	0.15 s	1.5 s	5.0 s	0.15 s	1.5 s	5.0 s
RTS	2.5	13.4	13.0	19.5	0.6	0.5	0.981	0.246	0.021
KF _{fb}	1.3	3.2	11.2	83.4	14.1	1.8	0.994	0.965	0.681
RTS + IMU	1.5	2.8	3.8	64.8	17.7	9.1	0.993	0.973	0.950

respectively), \mathbf{H}_k is changed based on the available observations. When both \mathbf{x}^k and a_x^k are available, we can write the matrix form of the eq. (33):

$$\begin{bmatrix} \mathbf{x}^k \\ a_x^k \end{bmatrix} = \begin{bmatrix} 1 & 0 & 0 \\ 0 & 0 & 1 \end{bmatrix} [\mathbf{x}^k \mathbf{v}_x^k a_x^k]^T + \eta_k \quad (34)$$

when only a_x^k is available, the matrix form of the eq. (33) is:

$$a_x^k = [0 \ 0 \ 1] [\mathbf{x}^k \mathbf{v}_x^k a_x^k]^T + \eta_{a,k} \quad (35)$$

The operation of Kalman filter has two steps: (**1) prediction or time update step and (**2) correction or measurement update. The procedure of KF is well described in [13,40].

3.2.2.5. Kf_{fb} trajectory. The results of the forward Kalman filter (KF trajectory) can be improved with a backward smoothing process using the Rauch-Tung-Striebel algorithm (KF_{fb} trajectory). We adopted the Rauch-Tung-Striebel algorithm described in [13]. The results of all trajectories are shown in Fig. 25, where REF, RTS, RTS + IMU, KF, and KF_{fb} trajectories are presented. The quality estimators for IMU, RTS, RTS + IMU, KF, and KF_{fb} trajectories are presented in Table 3. The RTS* represents the measured RTS points, without linear interpolation between points.

In Table 2 we can see, that the IMU trajectory is determined with the lowest accuracy ($RMSE_r = 5.2$ mm). The quality estimators for RTS* indicates that the measured RTS points are highly accurate ($RMSE_r = 1.6$ mm). However, due to the low frequency of the RTS measurement

according to the shake table's motion, the RTS trajectory do not represent the actual trajectory motion well ($RMSE_r = 2.5$ mm). When using the Kalman filter for IMU and RTS fusion, the position estimates (KF) can drift between the Kalman filter update steps, as shown in Fig. 25. Accuracy of the KF trajectory is low ($RMSE_r = 4.9$ mm). The RTS + IMU trajectory coincided with the reference trajectory (REF) much better. The accuracy is better, the SNR is higher and corr is closer to 1. The results of the KF_{fb} trajectory are even slightly better than those of the RTS + IMU trajectory. Both trajectories (RTS + IMU and KF_{fb}) reached better accuracy than the RTS trajectory ($RMSE_r = 1.5$ mm and $RMSE_r = 1.3$ mm). We can conclude that adding a low-cost IMU sensor to the kinematic RTS measurements can significantly improve the accuracy of the trajectory tracking. Based on the root-mean-square error, the combined trajectory accuracy was 40% better, and the SNR was more than three times higher than the RTS trajectory in our test.

In our laboratory experiment the average time between RTS measurements ($\bar{\Delta t}_{RTS}$) is about 0.15 s. Outdoors, where the conditions for kinematic RTS tracking measurements are not always perfect (poor geometry, larger distance between RTS and signal prism, interrupted signal or signal outages) the intervals between RTS measurements can be longer. In Fig. 26 and Fig. 27, we can see the results where the average time intervals between RTS measurements are 1.5 s and 5.0 s, respectively.

In Table 3 the quality estimators ($RMSE_r$, SNR, corr) of RTS, KF_{fb}, and RTS + IMU trajectories are presented.

Forward Kalman filtering with backward smoothing method per-

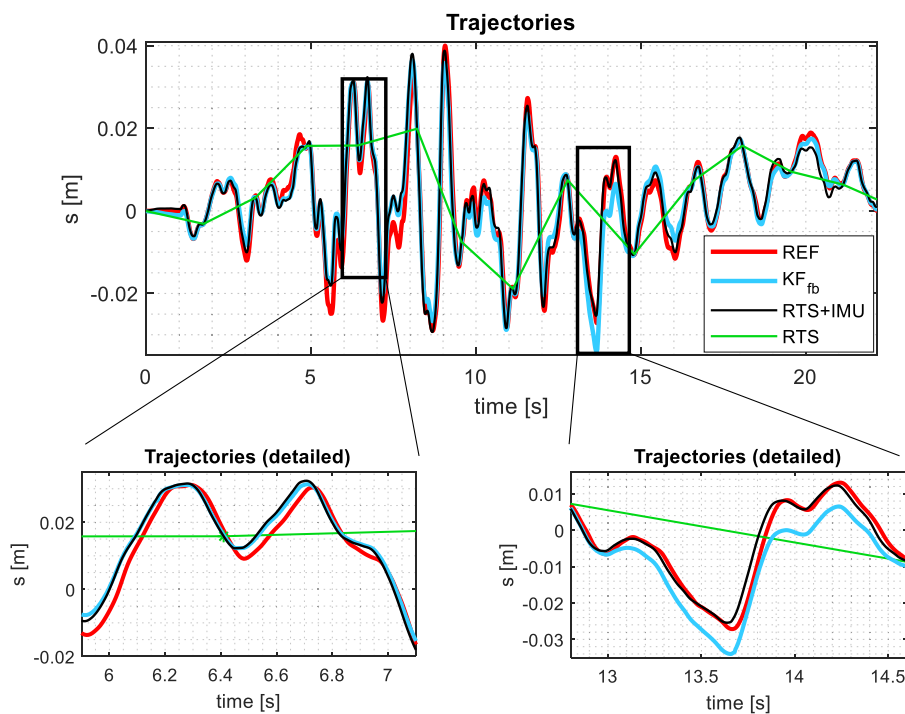


Fig. 26. Reference, KF_{fb}, RTS + IMU, and RTS trajectories (RTS measurement rate 1.5 s).

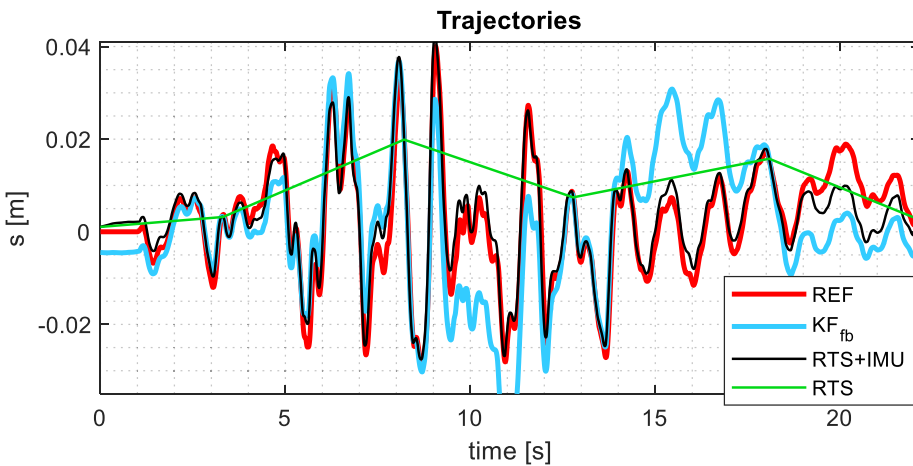


Fig. 27. Reference, KF_{fb}, RTS + IMU, and RTS trajectories (RTS measurement rate 5.0 s).

forms well, especially with short intervals between RTS measurements. At 0.15 s between the Kalman filter update steps, the results of KF_{fb} are slightly better than RTS + IMU, as we can see in Table 3. At a longer interval between the Kalman filter update steps, the RTS + IMU trajectory coincides much better with the reference trajectory than the KF_{fb} trajectory, as we can see in Fig. 26, Fig. 27, and Table 3. All quality estimators are better for the RTS + IMU trajectory; RMSE_r is smaller, SNR is higher and corr is closer to 1.

4. Conclusions

This paper examined the applicability of a low-cost IMU in determining the absolute position of an oscillating object. We have successfully developed a low-cost IMU module and a filtering procedure, which can be used for various applications. We demonstrated that the low-cost IMU sensor is suitable as a standalone sensor in monitoring applications where absolute positioning of an oscillating object is required. For this purpose, we evaluated the procedure of ZPF filtering the low-cost IMU measurements. The ZPF proved to be a powerful tool for eliminating the low-frequency errors (which accumulate enormous signal drifts) with zero phase shift. By using the ZPF, we successfully eliminated the drift caused by the signal noise of the accelerometer, as well as that caused by the third-order error accumulated by the bias error of the gyroscope. In the case of an oscillating object, the ZPF improved the accuracy of the object trajectory obtained by IMU measurements from a few hundred meters to a few centimeters. This method can provide a good and reliable low-cost monitoring system for oscillating objects in near real-time applications, where delayed results are sufficient.

When the object does not oscillate around the zero point, our proposed procedure can also be combined with low-frequency RTS kinematic measurements. As we have shown in the second experiment, the low-cost IMU measurements pre-processed with the ZPF filter can also significantly improve the RTS trajectory tracking results. The RTS measurements guarantee an absolute accuracy due to their highly accurate tracked points, while the IMU trajectory (after pre-processing) guarantees relative accuracy. With the proposed method, we detected the low-frequency and high-frequency movements of the object. By combining low-cost IMU and RTS measurements, we were able to obtain highly accurate measurement of the trajectory at a frequency of the IMU measurements. In our case, we improved the accuracy of the trajectory tracking compared to linear interpolation between measured RTS samples by 40% and the SNR (Signal-to-Noise Ratio) was more than three times higher. Usually, the fusion of high-rate IMU sensors and low-rate positioning systems (RTS, GNSS) is performed with a Kalman filter, where the quality of the results depends on the measurements update rate and the quality of the IMU [11,12]. At a higher update rate, the

forward Kalman filter with backward smoothing method performs well, which we also confirmed in our second experiment. It should be noted that both methods (ZPF and KF_{fb}) are suitable only for post-processing of finite signals. Nevertheless, our method has obvious advantages, because the results are more accurate even when low-grade IMU is used and the update rate of the kinematic RTS measurements is low or there are possible signal outages. However, in this paper we have shown that IMU measurements can significantly improve the kinematic RTS tracking measurement system accuracy. Further research should focus on investigating the limit of the length of the trajectory. We will also explore the possibilities of adapting the proposed method for use in near real-time applications.

Funding

The authors acknowledge the financial support of the Slovenian Research Agency (research core funding No. P2-0227 Geoinformation Infrastructure and Sustainable Spatial Development of Slovenia).

CRediT authorship contribution statement

Gašper Štěbe: Writing - original draft, Writing - review & editing. **Peter Krapež:** Writing - review & editing. **Janez Podobnik:** Writing - original draft, Writing - review & editing. **Dušan Kogoj:** Writing - original draft, Writing - review & editing.

Declaration of Competing Interest

The authors declare that they have no known competing financial interests or personal relationships that could have appeared to influence the work reported in this paper.

Acknowledgments

We acknowledge Jure Žižmond for the support in the fieldwork with Quanser Shake Table and Jernej Tekavec for sharing his experience with low-cost IMUs.

Appendix A. Supplementary material

Supplementary data to this article can be found online at <https://doi.org/10.1016/j.measurement.2021.109207>.

References

- [1] M. Gindy, R. Vaccaro, H. Nassif, J. Velde, A state-space approach for deriving bridge displacement from acceleration, *Comput. Civ. Infrastruct. Eng.* 23 (2008) 281–290, <https://doi.org/10.1111/j.1467-8667.2007.00536.x>.
- [2] K.T. Park, S.H. Kim, H.S. Park, K.W. Lee, The determination of bridge displacement using measured acceleration, *Eng. Struct.* 27 (2005) 371–378, <https://doi.org/10.1016/j.engstruct.2004.10.013>.
- [3] B. Lotfi, L. Huang, An approach for velocity and position estimation through acceleration measurements, *Measurement* 90 (2016) 242–249, <https://doi.org/10.1016/j.measurement.2016.04.011>.
- [4] H. Zhu, Y. Zhou, Y. Hu, Displacement reconstruction from measured accelerations and accuracy control of integration based on a low-frequency attenuation algorithm, *Soil Dyn. Earthq. Eng.* 133 (2020), <https://doi.org/10.1016/j.soildyn.2020.106122>.
- [5] J. Yang, J.B. Li, G. Lin, A simple approach to integration of acceleration data for dynamic soil-structure interaction analysis, *Soil Dyn. Earthq. Eng.* 26 (2006) 725–734, <https://doi.org/10.1016/j.soildyn.2005.12.011>.
- [6] N. Millor, P. Lecumberri, M. Gómez, A. Martínez-Ramírez, M. Izquierdo, Drift-free position estimation for periodic movements using inertial units, *IEEE J. Biomed. Heal. Informatics* 18 (2014) 1131–1137, <https://doi.org/10.1109/JBHI.2013.2286697>.
- [7] F. Gomez, J.W. Park, B.F. Spencer, Reference-free structural dynamic displacement estimation method, *Struct. Control Heal. Monit.* 25 (2018) 1–14, <https://doi.org/10.1002/stc.2209>.
- [8] Y. Gou, X. Shi, X. Huo, J. Zhou, Z. Yu, X. Qiu, Motion parameter estimation and measured data correction derived from blast-induced vibration: New insights, *Measurement* 135 (2019) 213–230, <https://doi.org/10.1016/j.measurement.2018.11.050>.
- [9] K. Matsuo, T. Miura, K. Tajima, Vibration reduction of a stepping motor using a pre-compensator to remove control delay, *IEEJ J. Ind. Appl.* 9 (2020) 191–192, <https://doi.org/10.1541/ieejia.9.191>.
- [10] B. Wu, T. Huang, Y. Jin, J. Pan, K. Song, Fusion of high-dynamic and low-drift sensors using kalman filters, *Sensors (Switzerland)* 19 (2019), <https://doi.org/10.3390/s19010186>.
- [11] A. Smyth, M. Wu, Multi-rate Kalman filtering for the data fusion of displacement and acceleration response measurements in dynamic system monitoring, *Mech. Syst. Signal Process.* 21 (2007) 706–723, <https://doi.org/10.1016/j.ymssp.2006.03.005>.
- [12] J. Kim, K. Kim, H. Sohn, Autonomous dynamic displacement estimation from data fusion of acceleration and intermittent displacement measurements, *Mech. Syst. Signal Process.* 42 (2014) 194–205, <https://doi.org/10.1016/j.ymssp.2013.09.014>.
- [13] C.M. Bishop, *Pattern recognition and machine learning*, Springer Science+Business Media, 2006. <https://doi.org/10.1109/TIT.1963.1057854>.
- [14] M. Omidalizandari, I. Neumann, E. Kemkes, B. Kargoll, D. Diener, J. Rüffer, J.-A. Paffenholz, Mems based bridge monitoring supported by image-assisted total station, in: *GeoSpatial Conf. 2019 – Jt. Conf. SMPR GI Res.*, Karaj, Iran, 2019, pp. 833–842.
- [15] B. Fang, W. Chou, L. Ding, An optimal calibration method for a MEMS inertial measurement unit, *Int. J. Adv. Robot. Syst.* 11 (2014) 14, <https://doi.org/10.5772/57516>.
- [16] D.W. Allan, Statistics of atomic frequency standards, *Proc. IEEE* 54 (1966) 221–230, <https://doi.org/10.1109/PROC.1966.4634>.
- [17] L. Ma, W. Chen, B. Li, Z. You, Z. Chen, Fast field calibration of MIMU based on the powell algorithm, *Sensors* 14 (2014) 16062–16081, <https://doi.org/10.3390/s140916062>.
- [18] V. Renaudin, M.H. Afzal, G. Lachapelle, Complete triaxis magnetometer calibration in the magnetic domain, *J. Sensors* 2010 (2010) 10, <https://doi.org/10.1155/2010/967245>.
- [19] C.M. Cheuk, T.K. Lau, K.W. Lin, Y. Liu, Automatic Calibration for Inertial Measurement Unit, in: *12th Int. Conf. Control. Autom. Robot. Vis.*, 2012: pp. 1341–1346. <https://doi.org/10.1109/ICARCV.2012.6485340>.
- [20] S. Bektas, Least square fitting of ellipsoid using orthogonal distances, *Bol. Ciências Geodésicas* 21 (2015) 329–339, <https://doi.org/10.1590/S1982-21702015000200019>.
- [21] S. Bektas, Orthogonal distance from an ellipsoid, *Bol. Ciências Geodésicas* 20 (2014) 970–983, <https://doi.org/10.1590/S1982-21702014000400053>.
- [22] M. Kok, T.B. Schön, Magnetometer calibration using inertial sensors, *IEEE Sens. J.* 16 (2016) 5679–5689.
- [23] J. Rohac, M. Sipos, J. Simanek, Calibration of low-cost triaxial inertial sensors, *IEEE Instrum. Meas. Mag.* (2015) 32–38, <https://doi.org/10.1109/MIM.2015.7335836>.
- [24] J. Botero-Valencia, D. Marquez-Viloria, L. Castano-Londono, L. Morantes-Guzmán, A low-cost platform based on a robotic arm for parameters estimation of Inertial Measurement Units, *Meas. J. Int. Meas. Confed.* 110 (2017) 257–262, <https://doi.org/10.1016/j.measurement.2017.07.002>.
- [25] E.M. Mikhail, F. Ackermann, *Observations and Least Squares*, 1978. [https://doi.org/10.1016/0031-8663\(78\)90007-8](https://doi.org/10.1016/0031-8663(78)90007-8).
- [26] W.T. Fong, S.K. Ong, a Y.C. Nee, Methods for in-field user calibration of an inertial measurement unit without external equipment, *Meas. Sci. Technol.* 19 (2008) 11. <https://doi.org/10.1088/0957-0233/19/8/085202>.
- [27] L. Ye, A. Argha, B.G. Celler, H.T. Nguyen, S.W. Su, Online auto-calibration of triaxial accelerometer with time-variant model structures, *Sens. Actuators A Phys.* A 266 (2017) 294–307, <https://doi.org/10.1016/j.sna.2017.08.049>.
- [28] V. V. Avrutov, P.M. Aksonenko, P. Henaff, L. Ciarletta, 3D-calibration of the IMU, in: *IEEE 37th Int. Conf. Electron. Nanotechnology, ELNANO 2017*, 2017, pp. 374–379. <https://doi.org/10.1109/ELNANO.2017.7939782>.
- [29] Z. Wu, W. Wang, Magnetometer and gyroscope calibration method with level rotation, *Sensors* 18 (2018) 18, <https://doi.org/10.3390/s18030748>.
- [30] N. Yadav, C. Bleakley, Fast calibration of a 9-DOF IMU using a 3 DOF position tracker and a semi-random motion sequence, *Measurement* 90 (2016) 192–198, <https://doi.org/10.1016/j.measurement.2016.04.066>.
- [31] Leica Geosystems, *GeoCOM Reference Manual – Version 1.50*, in: n.d.: p. 207.
- [32] S. Stancin, S. Tomažič, On the interpretation of 3D gyroscope measurements, *J. Sensors* 2018 (2018), <https://doi.org/10.1155/2018/9684326>.
- [33] A. Noureldin, T.B. Karamat, J. Georgy, *Fundamentals of Inertial Navigation, Satellite-based Positioning and their Integration*, Springer, 2013. <https://doi.org/10.1007/978-3-642-30466-8>.
- [34] R. Chow, Evaluating inertial measurement units, *TEST Meas. WORLD*, 2011, pp. 34–37.
- [35] J.O. Smith III, *Introduction to Digital Filters with Audio applications*, 2007.
- [36] F. Cohen Tenoudji, *Analog and Digital Signal Analysis From Basics to Applications*, Springer International Publishing Switzerland 2016, 2016. <https://doi.org/10.1007/978-3-319-42382-1>.
- [37] H.T. Toivonen, *Applied Signal Processing*, Åbo Akademi University, 2004.
- [38] S.K. Mitra, *Digital Signal processing - A Computer Based Approach*, McGraw-Hill, 1997.
- [39] R. Glaus, *Kinematic Track Surveying by Means of a Multi-Sensor Platform*, Swiss Federal Institute of Technology Zurich, 2006.
- [40] P.Y.C. Hwang, R. Grover Brown, *Introduction to Random Signals and Applied Kalman Filtering with MATLAB exercises*, John Wiley & Sons Inc, 2012.